Enhancement of the piezoelectric effect in Fe-substituted GaAsO 4 : a combined XRD, Raman spectroscopy and first principles study

D. Zheng, P. Roumanille, P. Hermet, M. Cambon, J. Haines, Olivier Cambon

Enhancement of the piezoelectric effect in Fe-substituted $GaAsO_4$: a combined XRD, Raman spectroscopy and first principles study.

*D. Zheng [1,2], P. Roumanille [2,3], P. Hermet[2], M. Cambon[2], J. Haines[2], O. Cambon[2]**

[1] School of Materials and Chemical Engineering, Xi'an Technological University, Shaanxi Key Lab Photoelect Funct Mat & Devices, Xian 710032, People's Republic of China

[2] Institut Charles Gerhardt Montpellier, UMR-CNRS-UM-ENSCM 5253, Université de Montpellier, Place E. Bataillon, 34095, Montpellier, Cedex 5, France.

[3] Institut de Recherche Technologique Antoine de St Exupéry, 3 rue Tarfaya, CS 34436, 31405 Toulouse cedex 4, France.

ABSTRACT

$GaAsO_4$ is the highest performance piezoelectric material of the $M^{III}X^{V}O_4$ alpha-quartz type group. First principles based calculations of the pure $FeAsO_4$ show that the piezoelectric properties are strongly improved by replacing Ga^{3+} by a chemical element of the d-bloc like Fe^{3+}.

For $GaAsO_4$, our calculations give, d_{11} =7.08 and d_{14} =5.76 pC/N, while these values are significantly higher in $FeAsO_4$ to reach d_{11} =18.77 and d_{14} = 13.78 pC/N; about a factor of three greater than in $GaAsO_4$ due to the increase of the elastic compliances of $FeAsO_4$ with respect to $GaAsO_4$. These results show that the electronic configuration and particularly the involvement of the *d*-orbitals in the *M*-O bonds in the $M^{III}O_4$ tetrahedron could be at the origin of this increasing. By considering a linear dependence of d_{11} or d_{14} between the parent compounds, $GaAsO_4$ and $FeAsO_4$**,** we get the following equations for the $Ga_{(1-x)}Fe_xAsO_4$ solid solution: d_{11} [pC/N] = 11.689 x_{Fe} + 7.082 and d_{14} [pC/N] = 8.021 x_{Fe} + 5.762. These predictions motivated the first synthesis of mixed $Ga_{(1-x)}Fe_xAsO_4$ solid solutions with x= 0,09; 0,18 and 0,45. The hydrated compounds, $Ga_{1-x}Fe_xAsO_4{,}2H_2O$, were obtained by hydrothermal synthesis and the alpha-quartz phases $Ga_{1-x}Fe_xAsO_4$ were crystallized with a thermal treatment in an oven at 600°C for 24h. XRD patterns show that the cell parameters are in accordance with a Vegard's law for the orthorhombic hydrated phases (*Pbca* space group) and for the trigonal dehydrated alpha-quartz phases ($P3_121$ space group). Raman spectroscopy data obtained for the hydrated phases confirm the results of the literature on $FeAsO_4{\cdot}2H_2O$, $GaAsO_4{\cdot}2H_2O$ and other arsenate analogues as well as their substituted analogs on the *M* and *X* sites. For the dehydrated alpha-quartz phases, all the main peaks observed in Raman spectra have been observed and the assigned by analyzing the experimental spectra measured in solid solutions and the calculated spectra in the parent end-

member compounds. DFT calculations were used to identify the Raman vibrational modes. As in the case of $GaAsO_4$, no libration mode of oxygen atoms is present for $FeAsO_4$ that could lead to a very high thermal stability. These results prove the interest of α-quartz type $Fe_xGa_{1-x}AsO_4$ solid solutions.

1. INTRODUCTION

Stability is one of the most important properties of piezoelectric materials from the point of view of current research and future applications [1, 2]. Physical properties of piezoelectric materials, such as dielectric, piezoelectric and electromechanical coupling coefficient etc., are often restricted by the thermal stability [3, 4]. Starting from the commonly used piezoelectric material, α-quartz itself, and GeO_2 to members of the α-Quartz-type family compounds with the general formula MXO_4 (M= Al, Ga, Fe, B, and X=P and As), research on their crystal structures, crystal growth conditions and piezoelectric properties has been carried out over the past decades [5, 6]. However, there are still some existing barriers limiting their piezoelectric performances and potential applications at high temperature [7, 8]. This has motivated the study of MXO_4 compounds. The α-quartz homeotypes MXO_4 belong to the $P3_121$ or $P3_221$ space groups. Their piezoelectric properties and thermal stability are closely related to the structural distortion of the α-phase with respect to the β-phase, and this structural distortion can be described by the intertetrahedral bridging angle θ and the tetrahedral tilt angle δ. Indeed, with the recent advances in research, some important empirical structure-property relationships for α-quartz homeotypes have been established between thermal stability, piezoelectric, physical properties and the distortion with respect to the β-quartz structure [9]. The piezoelectric coupling coefficient of these α-quartz homeotypes materials was found to be

a linear function as the structural distortion with respect to β-quartz structure and it increases with the structural distortion. For example, SiO_2 (θ=144.8°, δ=16.3°) and $AlPO_4$ (θ=142.8°, δ=17.6°), have phase transition temperatures of 573 and 586 °C respectively [10, 11], along with a higher degree of structural distortion (the bridging angle θ reduces while tilt angle δ increases) and their electromechanical coupling coefficient k increases from 8% to 11%. Similarly, $FePO_4$ (θ=137.8°, δ=21.5°) and $GaPO_4$ (θ=134.4°, δ=23.3°), which have a similar structure distortion, could have a similar piezoelectric coupling coefficient at room temperature of about k=16%. These two materials also have a good thermal stability up to temperatures of 707 and 927 °C respectively [12-14]. It is also reasonable to predicted that $GaAsO_4$, which possess the most distorted crystal structure (θ=129.6°, δ=26.9°), should exhibit the highest thermal stability (up to 1300 K) and the highest piezoelectric coupling coefficient (about 22%) [15]. Based on the above results, this paper describes the investigation of the most promising piezoelectric material by use of the chemical doping method, as chemical doping is a powerful tool to study physical and chemical properties of materials. It can bring about changes in conductivity, bond lengths, bond angles, lattice distortions and lattice parameters of the target materials depending upon the synthesis conditions. Accordingly, we used hydrothermal methods for preparing the $Ga_{1-x}Fe_xAsO_4$ series using iron lying in the same period of the periodic table of elements with a slightly larger radius than that of gallium to systematically dope or substitute gallium in the crystal structure of $GaAsO_4$. In fact, increasing the average ion size of *M* site cations of MXO_4 is one of the main ways to modify the structural distortion. Thus, we can investigate the important relationship between the crystal structural distortion and the chemical composition of the solid solution obtained in the process of materials synthesis and then integrate the design and synthesis of such tunable structures with adjustable physical properties in target α-quartz homeotype piezoelectric materials. All these

adjustable intrinsic properties of piezoelectric materials will provide excellent performance for future applications in high-temperature environments and in micro-electronic components requiring high frequencies and consequently miniaturization. Even in the field of second harmonic generation (SHG) these materials may be of great interest due to their expected nonlinear optical (NLO) properties [16].

2. EXPERIMENTAL AND METHODS SECTION

2.1. Sample Preparation.

Powders of the $Ga_{1-x}Fe_xAsO_4$ (x =0.11, 0.18, 0.60) solid solution series were synthesized by hydrothermal methods and followed by a subsequent heat treatment process. 7.7g (0.075mol) GaOOH and 40g (0.1mol) $Fe(NO_3)_3,9H_2O$ were separately dissolved in the arsenic acid solution (25ml H_3AsO_4 + 25ml H_2O). Next, when the two solutions were clarified, they were mixed them under continuous magnetic stirring. Finally, this mixture was transferred in a PTFE-lined autoclave, maintained at 170°C for 3 days and then gradually heated at about 5 degrees per day up to 245°C.

After rapid cooling, the solid precipitate was filtered, washed several times with distilled water and absolute ethanol and dried at 60 °C yielding the hydrated phases. The anhydrous α-quartz-type phases were obtained by heating the above powders in an oven at 600°C for 24h.

2.2. SEM AND EDX

The synthesized products were characterized using a scanning electron microscope (SEM) equipped with an Energy Dispersive X-Ray (EDX) analyzer to determine the chemical composition of the sample. A Quanta 200 field emission gun (FEI) equipped with an SDD diode was used as detector (Oxford INCA). Spectra were measured under a low vacuum at 15 kV. At least three different areas were checked for each sample. In this paper, the iron content *x* of three compositions studied was 0.11, 0.18 and 0.60 respectively. The sample $Ga_{0.40}Fe_{0.60}AsO_4$ and its hydrate are presented as examples with their EDS and SEM results in Figure S1 and Tables S1 (Supporting Information).

2.3. Powder XRD

The samples were characterized by X-ray diffraction (XRD) on a PanAnalytical X'Pert diffractometer equipped with an X'Celerator detector using Cu-Kα radiation ($K\alpha_1$ = 1.5405 Å, $K\alpha_2$ = 1.5444 Å). To eliminate the fluorescence due to the excitation of the iron in samples, a graphite monochromator was placed between the sample and the detector. The powder samples, which had been ground and passed through a 20-μm sieve, were placed in a rotating sample holder. The angular range investigated was as follows: 2θ = 7°-100°. Acquisition times were approximately 12 hours with a 0.008° step size. Le Bail fits and Rietveld refinements were performed with the FULLPROF program [17]. Quantitative analysis by two-phase Rietveld refinement indicated that the true compositions of the solid solutions are (x=0.09, 0.18, 0.45) with the remaining iron being found in a secondary pure iron end member phase (Details in SI).

2.4. Raman spectroscopy

Raman measurements were performed at room temperature on a Horiba Jobin-Yvon Labram Aramis Raman spectrometer equipped with a blue diode laser (λ = 473 nm). The powder was placed on a glass plate and the laser power was ~2 mW. The spectrometer was calibrated using samples of Si and $GaAsO_4$. The $Ga_{1-x}Fe_xAsO_4$ Raman lines were fitted using pseudo-Voigt functions. The spectral resolution is about $1cm^{-1}$.

2.5. First principles based calculations

Calculations for $GaAsO_4$ and $FeAsO_4$ were performed within the density functional theory (DFT) framework as implemented in the ABINIT package [18]. The all-electron potentials are replaced by norm-conserving pseudopotentials generated according to the Troullier-Martins scheme. Ga ($4s^2$, $3d^{10}$, $4p^1$), Fe ($3d^6$, $4s^2$), As ($4s^2$, $4p^3$) and O ($2s^2$, $2p^4$)-electrons are considered as valence states. The electronic wave functions are expanded in plane-waves up to a kinetic energy cutoff of 55 Ha. Lattice parameters and atomic positions were fully relaxed using a Broyden-Fletcher-Goldfarb-Shanno algorithm until the maximum stresses and residual forces were less than 7×10^{-4} GPa and 6×10^{-6} Ha/Bohr, respectively. Born effective charges, dielectric tensors, piezoelectric tensors and dynamical matrix (yielding the phonon frequencies and eigenvectors) were obtained within a variational approach to density functional perturbation theory whereas the Raman susceptibilities were calculated from a nonlinear response formalism taking advantage of the $2n$+1 theorem [19]. $GaAsO_4$ was studied using the generalized gradient approximation (GGA), according to the Perdew, Burke and Ernzerhof (PBE) parametrization[20], and a 10×10×6 mesh of special k-points[21]. This exchange-correlation functional gave an excellent prediction with the

experimental data for the study of crystallographic structure[22], lattice dynamics and piezoelectric properties in non-magnetic α-quartz-type $M^{III}X^{V}O_4$ compounds[6] with M = B, Al, Ga and X = P, As. In the case $FeAsO_4$, the primitive unit-cell has been doubled along the c-axis to impose an antiferromagnetic order. We found a magnetic moment on iron of 4.15 μ_B, which is in good agreement with the reported value[23] of 4.53 μ_B measured at 5 K for $FePO_4$. These values are consistent with a high spin $3d^5$ Fe^{3+} ion (5.92 μ_B) when extrapolated the experimental magnetic moment of $FePO_4$ at 0K. We used the local density approximation (LDA) according to the Perdew and Wang (PW) parametrization[24] and a 6×6×2 mesh of special k-points[21]. This change of functional with respect to $GaAsO_4$ is supported by a better description of the $FeAsO_4$ crystal structure that is the only experimental data known for this compound. Indeed, the LDA/PW relaxed lattice parameters of $FeAsO_4$ (a = 5.050 and c = 11.626 Å) are underestimated by less than 2% with respect to the experimental ones[25] (a = 5.154 and c = 11.470 Å). In contrast, the GGA/PBE relaxed ones (a = 5.277 and c = 12.084 Å) are overestimated by more than 5 % along c. Considering the strong correlation between the crystal structure and the piezoelectric efficiency in α-quartz-type $M^{III}X^{V}O_4$ compounds[6], prediction of the piezoelectric constants in $FeAsO_4$ could be less reliable at the GGA/PBE level. The piezoelectric constants of $Ga_{1-x}Fe_xAsO_4$ solid solutions have been estimated supposing a Vegard's law between the two parent compounds.

3. RESULTS AND DISCUSSION

3.1 Hydrated Phases

a. X-ray Powder diffraction

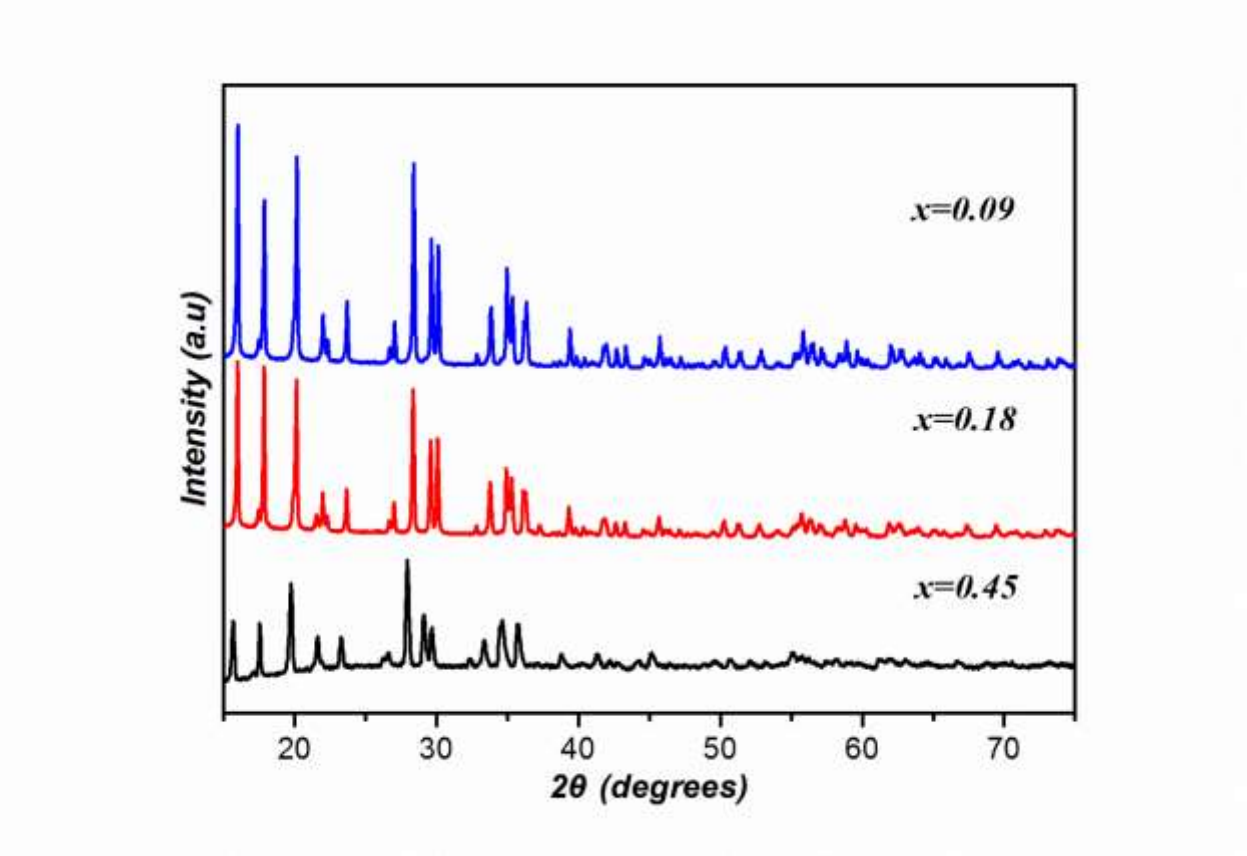

Fig. 1 XRD patterns of the as prepared $Ga_{1-x}Fe_xAsO_4,2H_2O$

Figure 1 shows the X-ray powder diffraction patterns of the hydrated phases $Ga_{1-x}Fe_xAsO_4,2H_2O$ (x =0.09, 0.18, 0.45) solid solution, space group *Pbca*, over the range of concentrations studied at ambient temperature. All the samples exhibit a good crystallinity. For the samples with lower iron content (x =0.09, 0.18), we can observe a set of diffraction peaks lying between those of orthorhombic $GaAsO_4 \cdot 2H_2O$ (JCPDS No. 026-0667) and orthorhombic $FeAsO_4,2H_2O$ (JCPDS No. 037-0468). At the same time, by comparing of diffraction peaks in Figure 1, we can observe that with the increase of iron content in the crystal structure of solid solution, changes have occurred in the unit cell parameters as shown by a shift of the diffraction peaks toward lower 2θ

angles when the iron content reaches a higher percentage such as x=0.45. This phenomenon is a consequence of the expansion of the $GaAsO_4,2H_2O$ unit cell due to the substitution of iron on the gallium sites.

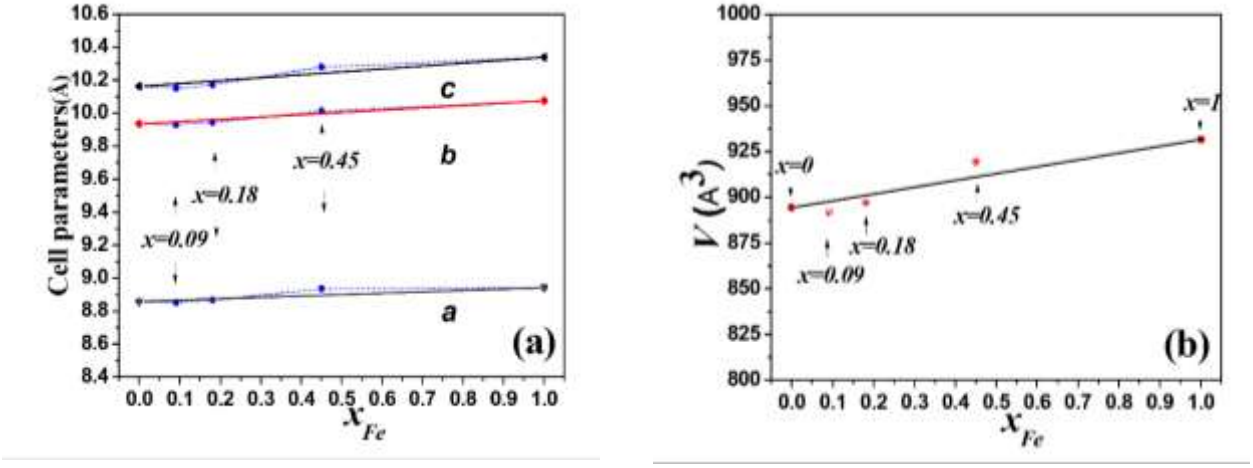

Fig. 2 Experimentally determined (a) lattice parameters and (b) cell volume *V* as a function of composition x in $Ga_{1-x}Fe_xAsO_4,2H_2O$. Solid lines show linearly interpolated values linking the $GaAsO_4,2H_2O$ and $FeAsO_4,2H_2O$ end members (Vegard's Law).

The orthorhombic lattice parameters *a*, *b* and c were calculated using Le Bail fits over the range $10° < 2\theta < 90°$. The values of *a*, *b* and *c* are plotted as a function of the Fe concentration *x* in the $Ga_{1-x}Fe_xAsO_4,2H_2O$ solid solution as shown in Figure 2(a). Among them, the data of the end members $GaAsO_4,2H_2O$ and $FeAsO_4,2H_2O$ come from the literature for comparison [26, 27]. Actually, the lattice parameters almost showed a linear change generally in line with Vegard's law for the present solid solution series. The small negative deviations from the Vegard's law are extremely small for $x<0.25$, while discernibly positive for $x>0.25$, resulting in the slight "S" shape of the unit-cell parameter-composition curves. Similar behavior occurs for the dependence of unit cell volumes *V* as a function of the Fe concentration in the solid solution as presented in Figure 2(b).

It is evident that the lattice parameters and unit cell volume of the synthesized phases are found to vary continuously as a function of composition between $GaAsO_4,2H_2O$ and $FeAsO_4,2H_2O$ end members. Because the non-bonding radius of Fe^{3+} (1.68 Å) is slightly larger than that of Ga^{3+} (1.63 Å), so it can reasonably deduced that the Fe–As distance should also be greater than that of Ga–As when Fe^{3+} ions are used to substitute Ga^{3+} in the $GaAsO_4,2H_2O$ structure. The lattice parameters and cell volume correspondingly increase with *x* giving rise to lattice expansion similar to previous reports on α-quartz-type homeotype phosphate solid solutions [28-31].

3.1.2 Raman Spectroscopy

The hydrated phases $Ga_{1-x}Fe_xAsO_4,2H_2O$ (x =0.09, 0.18, 0.45) were studied by Raman spectroscopy at room temperature. Generally, metal arsenates $M^{III}AsO_4,2H_2O$ (M^{III}: Ga or Fe) belong to the orthorhombic space group *Pbca* (= D_{2h}). The AsO_4^{3-} groups occupy the C_1 site symmetry in the crystal and the corresponding factor group analysis theoretically yields 9A modes, altogether 36 Raman active modes classified as $\Gamma(AsO_4^{3-}) = 9(A_g(Ra) + B_{1g}(Ra) + B_{2g}(Ra) + A_u(Silent) + B_{1u}(IR) + B_{2u}(IR) + B_{3u}(IR))$. According to previous related research work [32, 33], the arsenate bending and stretching vibrations modes of the gallium(III) arsenate dihydrate ($GaAsO_4,2H_2O$) and iron(III) arsenate dihydrate ($FeAsO_4,2H_2O$, scorodite) can all be distinctively observed in the Raman spectrum between 327 and 484 cm^{-1} and the region from 800 to 900 cm^{-1}, respectively. However, the position and intensity of their Raman lines also exhibit obvious differences in these two regions. For $GaAsO_4,2H_2O$, the strongest intense band occurring in the Raman spectrum at 894 cm^{-1} assigned to the $\nu_1(A_1)$ totally symmetric stretch and the bands at 861, 837, and 826 cm^{-1} ascribed to the $\nu_3(F_2)$ antisymmetric stretch. However, for $FeAsO_4,2H_2O$,

Gomez et al. [33, 34] assigned the most intense band observed in the Raman spectra around at 800 cm^{-1} to the $\nu_1(A_1)$ totally symmetric stretch and the bands at 880, 870, and 830 cm^{-1} to the $\nu_3(F_2)$ antisymmetric stretch. Savage et al. [35] and Myneni et al. [36] have different opinions on this assignment, they proposed that the most intense band at about 800 cm^{-1} should be an antisymmetric stretching mode associated with oxygen bridging between As and Fe (As-O-Fe). A shoulder at 831 cm^{-1} was assigned to the As-O-Fe symmetrical stretching mode and the weaker band at 893 cm^{-1} to a non-bridging oxygen that may be associated with crystal faces or defects. Actually, such problems with the mode assignments are understandable because of the changes in position and intensity may result from the interaction or mixing of vibration modes, especially when their energy regions are similar (e.g. ν_1 (A_1) and ν_3 (F_2) arsenate modes) depending on the orientation of the crystal with respect to the polarization and wavelength of the laser [37]. The present Raman spectroscopy study is a good reflection of this situation and illustrates these changes very well.

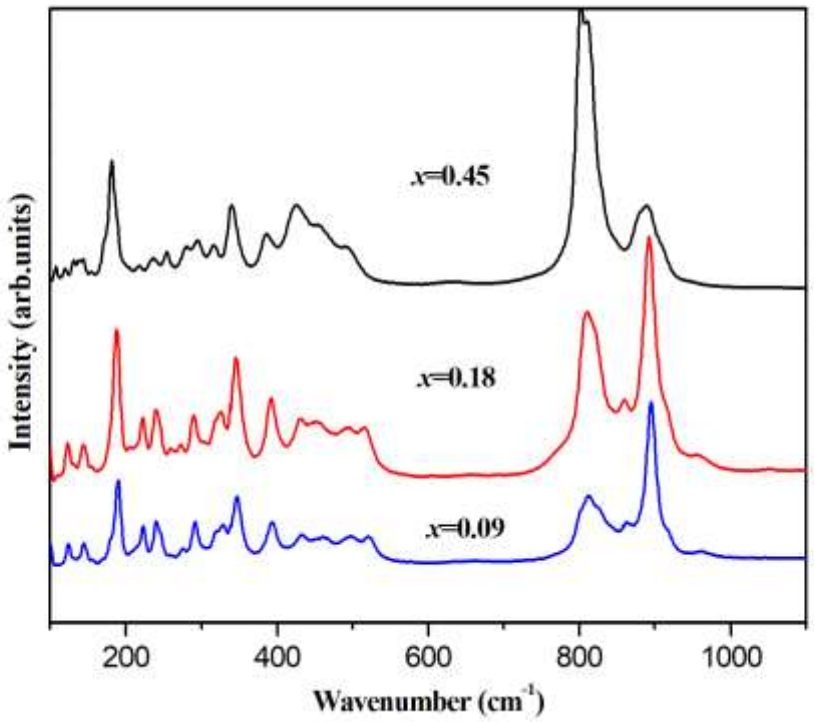

Fig. 3 Raman spectra of dihydrate compounds $Ga_{1-x}Fe_xAsO_4,2H_2O$ as a function of iron content

In this work, the Raman spectra of $Ga_{1-x}Fe_xAsO_4,2H_2O$ (x =0.09, 0.18, 0.45) are shown in Figure 3, firstly, most of the Raman line positions are quite similar and exhibit minor wavenumber downshifts as the iron content increases, likely related to the weakening of *M*–O bonds [31]. Significant changes in intensity are observed for the ν_1 (A_1) and ν_3 (F_2) arsenate modes between 800 and 900 cm^{-1} region. It appears that with the increase of iron content, the Raman line around 890 cm^{-1} gradually weakened and was no longer the most intense band; at the same time, the Raman line intensity near 810 cm^{-1} increased and became the strongest peak. If we compare the Raman line in this region with their parent compound ($GaAsO_4,2H_2O$) and the end member ($FeAsO_4,2H_2O$), our iron-doped products $Ga_{1-x}Fe_xAsO_4,2H_2O$ (x =0.09, 0.18, 0.45) perfectly demonstrated intermediate cases concerning the peak intensities of the Raman active stretching

modes observed between 800 and 900 cm^{-1}. This explains very well when the gallium in the crystal structure of $GaAsO_4,2H_2O$ is gradually replaced by iron. In the Raman spectrum the intensity of the original ν_1 (A_1) (totally symmetric stretch vibration) peak gradually decreases, while the intensity of ν_3 (F_2) (antisymmetric stretch vibration) peak increases. All this will cause the original ν_1 (A_1) of $GaAsO_4,2H_2O$ to weaken and be replaced by the antisymmetric stretching vibration of the $FeAsO_4,2H_2O$, and the original ν_3 (F_2) of the $GaAsO_4,2H_2O$ is replaced by the strongest peak, that is the symmetric stretch vibration of $FeAsO_4,2H_2O$. This also in line with the point of view of Nakamoto et al. [38] and Gomez et al. [33], that the symmetric stretching vibrations, which is a breathing type of mode, are always stronger than the antisymetric vibrations in terms of Raman intensity. The ν_1 (A_1) (totally symmetric stretch vibration) peak should thus exhibit the strongest Raman intensity with respect to the ν_3 (F_2) (antisymmetric stretch vibration) peaks. This fact has been confirmed by many articles on the Raman spectroscopy of $FeAsO_4,2H_2O$, $GaAsO_4,2H_2O$ and other arsenate analogues, as well as their substituted analogs on the *M* and *X* sites, which behave as those in the present study.

Table 1. Raman spectral of the arsenate vibrations modes for $Ga_{1-x}Fe_xAsO_4,2H_2O$

x=0 (ref.33)	*x*=0.09	*x*=0.18	*x*=0.45	*x*=1 (ref.34)	Band assignment (AsO_4^{3-})
894	895 812	892 810	888 802	 800	$\nu_1(A_1)$
861,837,826	863,849	860, 846	888,860,810	880,870, 830	$\nu_3(F_2)$
460,433	460, 431	451,431	485,451,424 ,	483,450,420	$\nu_4(F_2)$
394,346,327	393, 347, 337,328	392,346,337 ,325,	385,340,	380,340	$\nu_2(F_2)$
290,273,240, 222,189	290,274, 240,222, 190	289, 272, 261, 239,222, 206, 188	316,295, 280,253,235 ,216,180	315,292, 280,250,235, 215, 181	External and Lattice Modes

Correspondingly, for the bending modes, from the Table 1 we can see that the ν_4 (F_2) antisymetric mode of $GaAsO_4,2H_2O$ and $FeAsO_4,2H_2O$ are located at 460, 433 cm^{-1} and 483, 450, 420 cm^{-1} according to the references, while the ν_2 (F_2) vibrations are located at 394,346, 327 cm^{-1} and 380, 340 cm^{-1}, respectively. We can also observe the Raman spectra of all the above arsenate bending ν_4 (F_2) and ν_2 (F_2) modes as well as the external and lattice modes for our synthetic iron-doped dihydrate compound $Ga_{1-x}Fe_xAsO_4,2H_2O$ (x =0.09, 0.18, 0.45) are located just between their parent compound ($GaAsO_4,2H_2O$) and the end-member compound ($FeAsO_4,2H_2O$), which is showing a perfect evolution of the trend. The detailed stretching, bending vibration modes and lattice modes of the arsenate in different regions of the Raman spectrum for synthetic dihydrate compounds $Ga_{1-x}Fe_xAsO_4,2H_2O$ (x =0.09, 0.18, 0.45) are provided in Figures S3 and S4 (Supporting Information).

3.2 Dehydrated Phases with Alpha-Quartz Structure

3.2.1 XRD data

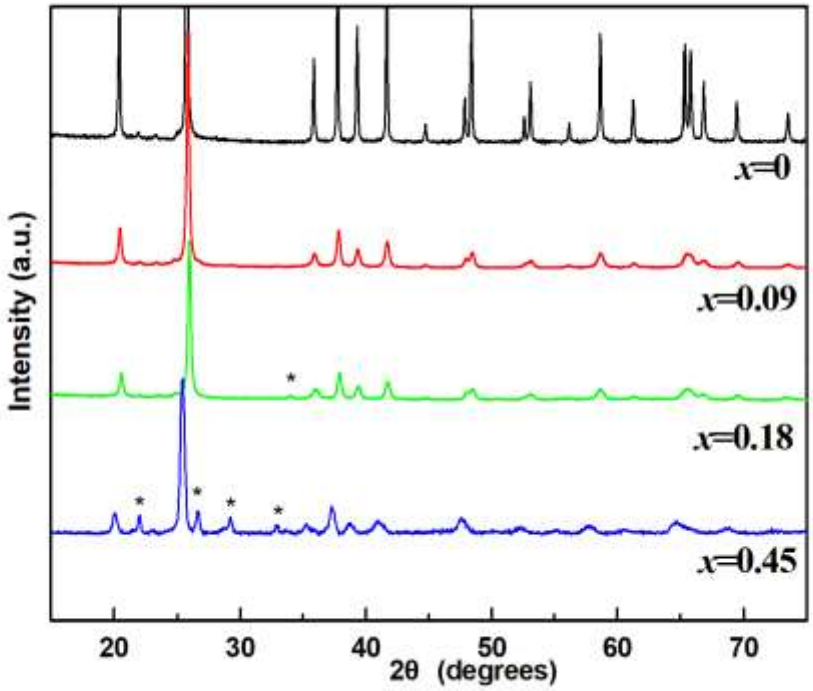

Fig. 4 XRD patterns of the as prepared $Ga_{1-x}Fe_xAsO_4$ (see text for meaning of the asterisks)

Heating the above hydrated phases $Ga_{1-x}Fe_xAsO_4,2H_2O$ in an oven at 600°C for 24h leads to the loss of their crystalline water yielding the corresponding dehydrated α-quartz-type trigonal ($P3_121$ space group) phases $Ga_{1-x}Fe_xAsO_4$ (x=0.09, 0.18, 0.45). The X-ray diffraction patterns of these dehydrated phases and the anhydrous $GaAsO_4$ for comparison are presented in Figure 4. From above XRD pattern, we can see that the diffraction patterns are very similar to that of the trigonal ($P3_121$) $GaAsO_4$ end member. However, there are several additional Bragg reflections (marked with asterisk in figure 4) in the diffraction patterns for iron contents of x= 0.09 and x=0.45, respectively, which correspond to reflections of monoclinic $FeAsO_4$ (See SI). This may suggest that the monoclinic $FeAsO_4$ phase found by XRD analysis is mainly derived from the dehydration

of the corresponding hydrated phase, which loses its structural water during the higher temperature treatment and finally leads to a nucleation and growth decomposition mechanism [31, 32]. At the same time, it is evident that all diffraction peaks shift to lower 2θ values with increasing x in $Ga_{1-x}Fe_xAsO_4$, indicating the lattice expansion of the $GaAsO_4$ unit cell caused by incorporation of iron on gallium sites.

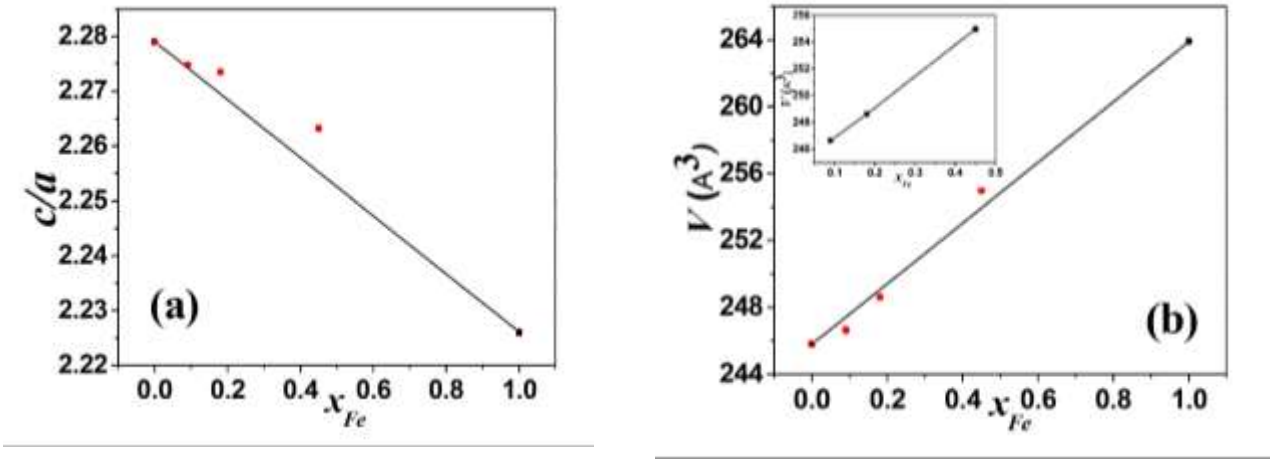

Fig. 5 c/a ratio (a) and unit cell volume (b) as a function of iron content in $Ga_{1-x}Fe_xAsO_4$. For pure $GaAsO_4$, the data come from ref 24 and for pure $FeAsO_4$ the data are the theoretical values calculated in this paper.

The detailed effects of this incorporation of iron on the unit-cell parameters of the $Ga_{1-x}Fe_xAsO_4$ trigonal ($P3_121$) solid solutions are shown in Fig. 5. Among them, the data of the end members $GaAsO_4$ and $FeAsO_4$ come respectively from the literature[25] and theoretical calculations for comparison. Firstly, it can be clearly seen from Fig. 5 (a) that the lattice parameter c/a ratio of the solid solutions decreases monotonously with *x*, while the behavior of the unit cell volumes is opposite, increasing with *x* (Fig. 5 (b)). This means that the lattice of $Ga_{1-x}Fe_xAsO_4$ expands as Fe^{3+} with a larger ionic radius substitutes for Ga^{3+} in $GaAsO_4$, but the increase of the *a* parameter value is larger than that of *c* parameter. However, the unit cell volume does not vary linearly with

the composition x between the $GaAsO_4$ and $FeAsO_4$ end members nor does the lattice parameter c/a ratio. In general, the values of c/a lie a little slightly above that expected by linear interpolation between limiting values for $GaAsO_4$ and $FeAsO_4$, while the volumes display a fluctuation with changes in iron content. Secondly, in detail, the deviation from the Vegard's law are extremely small for the trigonal ($P3_121$) solid solutions with x=0.09 and 0.18, but for the sample with x = 0.45, the deviation is a little larger. However, when the $GaAsO_4$ and $FeAsO_4$ end members are excluded, the unit cell volume of $Ga_{1-x}Fe_xAsO_4$ (x=0.09, 0.18, 0.45) exhibits an approximate linear increase as a function of composition x (Fig. 5 (b)). Upon incorporation of the larger Fe^{3+} cations on Ga^{3+} sites in the $Ga_{1-x}Fe_xAsO_4$ under the current reaction conditions, the increasing of the M–As non-bonding distance leads to a larger unit cell volume and further to a decrease of degree of structural distortion, which corresponds to an increase in the inter-tetrahedral bridging angle θ and a decrease in the tetrahedral tilt angle δ with x. This approximate linear evolution relationship of the unit cell volume as a function of x (Fig. 5 (b)) is especially useful to estimate the iron content in the $Ga_{1-x}Fe_xAsO_4$ solid solutions.

3.2.2 Raman Spectroscopy

According to group theory predicts, $Ga_{1-x}Fe_xAsO_4$ belongs to space group trigonal $P3_121$ or $P3_221$ (Z = 3) and will exhibit 54 modes of vibration:

$$\Gamma = 8A_1 + 10A_2 + 18E$$

Among them $8A_1 + 17E$ are predicted to be Raman active. The resulting Raman measurements of the $Ga_{1-x}Fe_xAsO_4$ samples along with the spectra of undoped compound $GaAsO_4$ for comparison are shown in Figure 6.

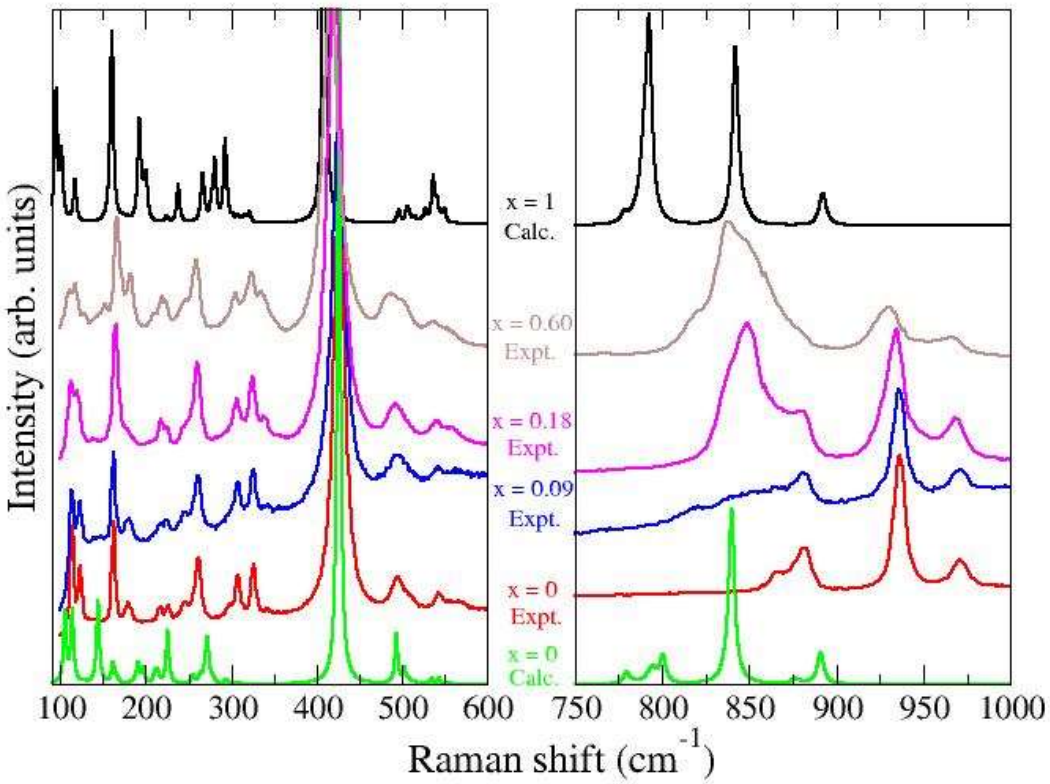

Fig. 6 Raman spectra of $Ga_{1-x}Fe_xAsO_4$ solid solutions as a function of iron content

Although the profiles of these spectra are very similar, there are still a few significant changes in the position and the relative intensity of several peaks as the iron content increases. In order to better understand these subtle changes, we divide the spectra into three wavenumber ranges: (i) A series of weaker lines below 400 cm^{-1}, (ii) a very intense line along with several weak lines between 400 and 600 cm^{-1}, and (iii) several strong lines with significant changes in intensity and line width

within the 800–1000 cm^{-1} range. According to previous reports [39, 40], for $GaAsO_4$, similar to other related α-quartz-type materials, such as $FePO_4$ and $GaPO_4$, the A_1 mode near 260 cm^{-1} involving oxygen displacements is not a libration, but is a more complex mode relate to bending of the various inter- and intratetrahedral angles caused by different components of O atoms displacements in different planes in the structure [41]. The Raman modes (cm^{-1}) of α-quartz-type $Ga_{1-x}Fe_xAsO_4$ solid solutions as a function of composition are listed in Table 2.

Table 2. Main frequencies (in cm^{-1}) observed in Raman spectra of α-quartz-type $Ga_{1-x}Fe_xAsO_4$ solid solutions.

Proposed Assignment	$x = 0$ Calc.	$x = 0$ Exp.	$x = 0.09$ Exp.	$x = 0.18$ Exp.	$x = 0.45$ % Exp.	$x = 1$ Calc.
E (TO+LO)	75					58
E (TO+LO)	105	114	113	113	111	96
A_1	114	123	123	120	118	101
E (TO+LO)	128	130		138	128	117
					152	
A_1	144	162	163	165	166	160
E (TO+LO)	162	180	180	179	182	166
					208	
E (TO+LO)	191	217	217	217	219	193
E (LO)	198	226	227	226	223	200
E (TO+LO)	212	245	245	245	246	223
A_1	226	262	262	261	258	238
E (TO+LO)	255	308	308	307	305	268
E (TO+LO)	264	323	322	322	319	277
A_1 + E (TO+LO)	272	326	326	325	324	280
E (TO)	295	343	343	338	336	293
A_1[(a)]	426	426	426	422	416	409
E (TO+LO)	493	494	494	492	486	495
E (LO)	503	508	506	506	502	506
A_1	534	542	542	540	538	537
E (TO+LO)	544	569	559	559	554	542
A_1 + E (TO+LO)	775-809	850-900	800-900	830-900	800-900	792
A_1 + E (TO+LO)	840	937	936	935	930	842
E (TO+LO)	890	971	970	969	966	892

(a) Intratetrahedral bending mode

Most of Raman lines exhibit a progressive change in wavenumber as the iron content increases. Figure 6 shows the evolution of the position of the Raman lines. The Raman shifts of the A_1 mode centered at 260 cm^{-1} and bending modes at 425 cm^{-1} have a slight downshift with increasing *x*, which is related to the weakening of the *M*–O bonds.

The DFT calculations demonstrated the absence of pure libration of the oxygen atoms in $GaAsO_4$ [16] and $FePO_4$ [39]. The calculated low frequency A_1 mode at 226 cm^{-1} for $GaAsO_4$ and 193cm^{-1} for $FePO_4$ involving the simultaneous displacement of the cations and the oxygen atoms. This mode exhibits strong damping prior to the α-β quartz transition in $FePO_4$ linked to a high degree of dynamic disorder. In the case of $FeAsO_4$ (Figure 7), the pure libration mode of the oxygen atoms is also absent.

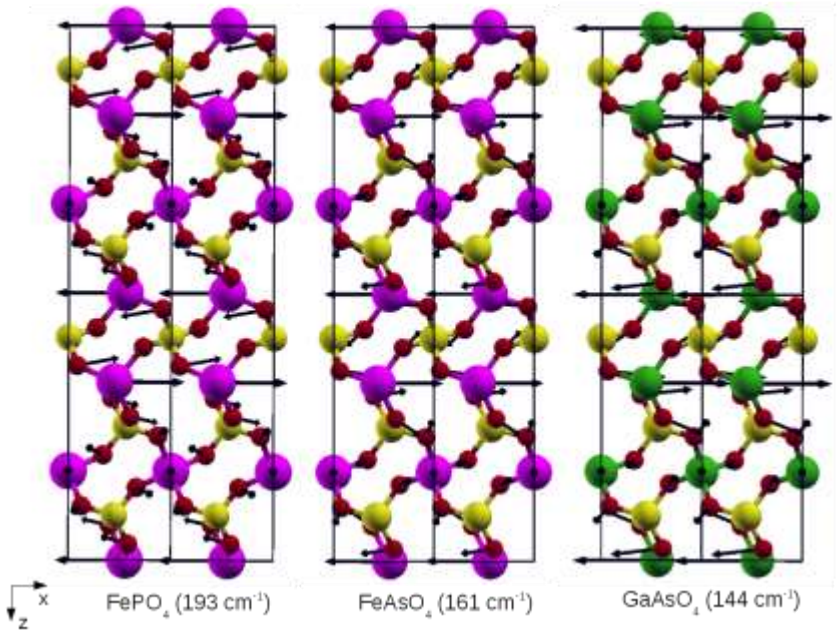

Fig 7. Calculated A_1 vibrational modes of $FePO_4$, $FeAsO_4$, and $GaAsO_4$ at 0 K. Large purple, medium yellow, and small red spheres represent (Fe, Ga), (P, As) and O atoms, respectively.

3.2.3 Piezoelectric properties

In the case of $GaAsO_4$ and $FeAsO_4$ α-quartz-type compounds, the piezoelectric-stress tensor has only two independent elements, namely $e_{11} = -e_{12} = -e_{26}$ and $e_{14} = -e_{25}$. Their magnitudes, given in Table 3, show that the substitution of Ga by Fe-atoms has only a small effect on the overall piezoelectric-stress components: $e_{11} \sim 0.215$ and $e_{14} \sim 0.145$ C/m^2. Their decomposition into a clamped-ion and an internal-strain contributions, such as [6], $e_{1\nu} = e_{1\nu}^{cl} + e_{1\nu}^{str}$ where $\nu = 1$ or 4 in Voigt notation, show a larger effect between these two compounds. Indeed, the magnitude (in absolute value) of the clamped-ion and internal-strain contributions are significantly higher in $FeAsO_4$ than in $GaAsO_4$ both for e_{11} and e_{14}. The higher electronic polarizability in $FeAsO_4$ associated with the d-orbitals is responsible of the increase of the clamped-ion contributions while the lower frequencies observed in $FeAsO_4$ explain the higher internal-strain contributions as $e^{str} \propto \omega_j^{-2}$ where ω_j is the frequency of the normal mode j. The decrease in frequencies observed in $FeAsO_4$ could be attributed to the decrease of the Fe-O interatomic force constants as the Fe-O distances (~1.90 Å) are longer than the Ga-O distances (~1.84 Å). For both compounds, the overall piezoelectric-stress values are dominated by the internal-strain contribution and the clamped-ion contribution decreases the magnitude of e_{11} or e_{14} by its negative sign. Thus, the increase of the e^{str} contribution in $FeAsO_4$ is pretty much offset by the increase of the e^{cl} contribution, leading to an overall value of e_{11} and e_{14} similar to those predicted for $GaAsO_4$ (Table 3). In contrast to α-quartz where the e_{14} value is very small [42] (-0.04 C/m^2), we highlight that this value is non negligible (~0.15 C/m^2) in the case of $FeAsO_4$ or $GaAsO_4$.

Compound	e_{11}			e_{14}		
	Clamped-ion	Internal-strain	Total	Clamped-ion	Internal-strain	Total
$GaAsO_4$	-0.20	0.42	0.22	-0.13	0.29	0.16
$FeAsO_4$	-0.33	0.54	0.21	-0.19	0.32	0.13

Table 3. Calculated independent piezoelectric-stress constants (C/m^2) in $GaAsO_4$ and $FeAsO_4$.

The piezoelectric-strain constants, d_{11} and d_{14}, are also of primary importance for piezoelectric devices as they are related to the athermal AT-cut, where the shift of the resonance frequency is minimal as a function of temperature. They are defined by: $d_{11} = e_{11}(S_{11} – S_{12}) + e_{14}\, S_{14}$ and $d_{14} = 2\, e_{11}\, S_{14} + e_{14}\, S_{44}$, where S is the compliance tensor defined under the condition of zero electric field (see Table 4). For $GaAsO_4$, our calculations give d_{11} =7.08 and d_{14} =5.76 pC/N, while these values significantly increase in $FeAsO_4$ to reach d_{11} =18.77 and d_{14} = 13.78 pC/N; about three times higher than in $GaAsO_4$. Thus, the highest piezoelectric-strain values predicted in $FeAsO_4$ are related to the increase of the elastic compliances with respect to $GaAsO_4$ as the piezoelectric-stress values are similar for the two compounds. This softening of the network in $FeAsO_4$ is associated with less rigid tetrahedra where the Fe-O and Fe-As distances are longer than Ga-O and Ga-As distances in the tetrahedra of $GaAsO_4$**.** Similar to Vegard's law observed for the lattice parameters (Fig. 5), we can estimate the piezoelectric-strain values of the $Ga_{1-x}Fe_xAsO_4$ solid solutions considering a linear dependence of d_{11} or d_{14} between the parent compounds, $GaAsO_4$ and $FeAsO_4$**.** Within this assumption, we get the following equations: d_{11} [pC/N] = 11.689 x_{Fe} + 7.082 and d_{14} [pC/N] = 8.021 x_{Fe} + 5.762. Thus, the d_{11} value could reach 8.1, 9.2 and 12.3 pC/N for an iron concentration of 9, 18 and 45 %, respectively. For these concentrations, the d_{14} values could reach 6.4, 7.2 and 9.4 pC/N, respectively. The comparison of these values with other α-quartz-type $M^{III}X^{V}O_4$ compounds[6] shows that, even with 1 %at. of iron, the d_{11} estimation of $Ga_{1-x}Fe_xAsO_4$

solid solutions are much higher than that reported in $AlPO_4$ and $GaPO_4$ (see Table 5). In the case of $GaAsO_4$, the $Ga_{1-x}Fe_xAsO_4$ solid solutions begin really interesting from 20 % iron doping (d_{11}^{calc} = 9.42 pC/N) and can reach d_{11}^{calc} = 18.77 pC/N for the pure $FeAsO_4$ end member. Similar observations can be seen about the d_{14} piezoelectric value. Note that powder of $FeAsO_4$ has been already synthesized which is the first step for a future growth of a single crystal.

All these calculated values of the piezoelectric constants will have to be confirmed by experimental piezoelectric measurements which are only possible on millimeter sized single crystals whose growth requires several years of technical development to get crystals of sufficient quality for measuring the true values of the piezoelectric constants. Moreover, these results show the interest to substitute M^{III} *p*-elements like Ga^{3+} by *d*-elements like Fe^{3+} to form chemical bonds with *d*-orbitals leading to decreasing the elastic constants values and increasing the d_{11} piezoelectric constant. Indeed, with the same M^{V} p-element (P or As), the d_{11} is about 2.5 times higher when Ga^{3+} is replaced by Fe^{3+}. This *d*-hybridation could be one of the keys to increase the piezoelectric performance of the materials.

	$GaAsO_4$	$FeAsO_4$
S_{11}	2.379	5.577
S_{12}	-0.738	-3.132
S_{13}	-0.403	-0.563
S_{14}	0.008	0.340
S_{33}	1.323	1.775
S_{44}	3.607	9.353
S_{66}	6.234	17.419

Table 4. Calculated independent compliance constants defined under the condition of zero electric field ($x10^{-2}$ GPa^{-1}).

	e_{11} (C/m^2)		d_{11} (pC/N)	
	Exp. [300 K]	Calc. [0 K]	Exp. [300 K]	Calc. [0 K]
$AlPO_4$	0.14[43], 0.16[44]	0.14[6]	3.3[44]	2.7[e]
$GaPO_4$	0.21[45]	0.22[6]	4.5[44,45]	4.8[6]
$GaAsO_4$	-	0.21[6]	5.5[46]	7.1[6]
$FePO_4$	-	0.18[47]	-	12.3[47]
SiO_2	0.15[48], 0.17[49]	0.15[6]	2.3[50]	2.1[6]

Table 5. Experimental and calculated e_{11} and d_{11} piezoelectric constants (SiO_2 is reference material).

4. CONCLUSIONS

In this work, the orthorhombic di-hydrate phases $Ga_{1-x}Fe_xAsO_4 \cdot 2H_2O$ and the dehydrated α-quartz-type trigonal $Ga_{1-x}Fe_xAsO_4$ solid solution series were synthesized by hydrothermal methods with a subsequent heating treatment. All the samples were studied as a function of composition by X-ray diffraction and Raman spectroscopy. The results show that all the members of the solid solution series were found to exhibit some very interesting gradual evolution in terms of lattice parameters as a function of the iron content in the corresponding structure.

From DFT calculations, it was shown that pure libration mode of oxygen atoms is absent in $FeAsO_4$. This suggests that the α-β quartz transition should be absent as in the case of $GaAsO_4$. Piezoelectric properties of $FeAsO_4$ were predicted by DFT calculations. The piezoelectric-strain constants are 18.77 and 13.78 pC/N for d_{11} and d_{14} respectively. These values are the highest values presently obtained in the α-quartz type family making the iron-substituted $Fe_xGa_{1-x}AsO_4$ of great interest for potential applications.

ASSOCIATED CONTENT

Supporting Information. Supplementary data are given in the Supporting Information file.

Table S1 and Fig S1. SEM photographs and Atomic composition from EDS analysis of $Ga_{(1-x)}Fe_xAsO_4$ and $Ga_{(1-x)}Fe_xAsO_4$, $2H_2O$ (with x= 0,6).

Fig. S2. XRD powder diffraction of $Ga_{(1-x)}Fe_xAsO_4$ (x= 0,6). Two phase Rietveld refinements were performed in order to estimate the quantity of monoclinic ($P2_1/n$) $FeAsO_4$ present in the dehydrated samples. The final value of x is then 0.45 in the alpha-quartz phase.

Fig. S3 Raman spectra of the arsenate stretching modes for synthetic dihydrate compound, $Ga_{1-x}Fe_xAsO_4 \cdot 2H_2O$.

Fig. S4 Raman spectra of the arsenate bending and lattice modes for synthetic dihydrate compounds $Ga_{1-x}Fe_xAsO_4 \cdot 2H_2O$

AUTHOR INFORMATION

Corresponding Author

* Author to whom correspondence should be addressed: O.Cambon, olivier.cambon@umontpellier.fr

Present Addresses

[1] Present address: School of Materials and Chemical Engineering, Xi'an Technological University, Shaanxi Key Lab Photoelect Funct Mat & Devices, Xian 710032, People's Republic of China

[2] Institut Charles Gerhardt Montpellier, UMR-CNRS-UM-ENSCM 5253, Université de Montpellier, Place E. Bataillon, 34095, Montpellier, Cedex 5, France.

[3] Institut de Recherche Technologique Antoine de St Exupéry, 3 rue Tarfaya, CS 34436, 31405 Toulouse cedex 4, France.

Author Contributions

The manuscript was written through contributions of all authors. All authors have given approval to the final version of the manuscript. These authors contributed equally.

Funding Sources

Any funds used to support the research of the manuscript should be placed here (per journal style).

Notes

Any additional relevant notes should be placed here.

ACKNOWLEDGMENT

This work was financially supported by national foundation for study abroad of China and the Natural Science Foundation of Shaanxi Province (No. 2015JM2065).

REFERENCES

[1] D. Damjanovic, N. Klein, J. Li et *al*., *Functional Materials Letters* **1**, 5-13 (2010).

[2] D. Maurya, M. Peddigari, Kang M.G. et *al.*, *Journal of Materials Research* **16**, 2235-2263 (2018).

[3] S. Zhang, F. Yu, *Journal of the American Ceramic Society* **10**, 3153-3170 (2011).

[4] H. Yang, C. Zhou, X. Liu et *al*., *Journal of the European Ceramic Society* **6**, 1177-1183 (2013).

[5] P. Labeguerie, M. Harb, I. Baraille et *al.*, *Phys. Rev. B* **81**, 045107:1–045107:9 (2010).

[6] P. Hermet, J. Haines, J.P. Aubry, O. Cambon, *Journal of Physical Chemistry C* **47**, 26645-26651 (2016).

[7] O. Cambon, J. Haines, *Crystals* **7**, 38 (2017).

[8] H.J. Lee, S. Zhang, Y. Bar-Cohen et *al., Sensors* **8**, 14526-14552 (2014).

[9] B.I. Kidyarov, V.V. Atuchin, N.V. Pervukhina, *Journal of structural chemistry* **6**, 1119-1125 (2010).

[10] K. Kihara, *European Journal of Mineralogy* **2**, 63-78 (1990).

[11] I.V. Veksler, R. Thomas, R. Wirth, *Am. mineral.* **88**, 1724-1730 (2003).

[12] M. Smirnov, N. Mazhenov, N. Aliouane, P. Saint-Grégoire, *J. Phys.: Condens. Matter* **22**, 225403−225413 (2010).

[13] H. Nakae, K. Kihara, M. Okuno, S. Hirano, S., *Zeitschrift für Kristallographie* **10**, 746-753 (1995).

[14] J. Haines, O. Cambon, N. Prudhomme, G. Fraysse, D.A. Keen, L.C. Chapon, M.G. Tucker, *Phys. Rev. B* **73**, 014103−014110 (2006).

[15] O. Cambon, G.M. Bhalerao, D. Bourgogne, J. Haines, P. Hermet, D.A. Keen, M.G. Tucker, *J. Am. Chem. Soc.* **133**, 8048–8056 (2011).

[16] P. Hermet, M. Souleiman, D. Clavier, B. Hehlen, C. Levelut, P. Sans, J. Haines, O. Cambon, *J. Phys. Chem. C* **119**, 8459−8464 (2015).

[17] J. Rodrigues-Carvajal, FULLPROF, a Rietveld refinement and pattern matching analysis program (2000).

[18] X. Gonze, B. Amadon, P.M. Anglade, J.M. Beuken, F. Bottin, P. Boulanger, F. Bruneval, D. Caliste, R. Caracas, M. Cote, T. Deutsch, L. Genovese, P. Ghosez, M. Giantomassi, S. Goedecker, D. Hamann, P. Hermet, F. Jollet, G. Jomard, S. Leroux, M. Mancini, S. Mazevet, S.; M.J.T. Oliveira, G. Onida, Y. Pouillon, T. Rangel, G.M. Rignanese, D. Sangalli, R. Shaltaf, M. Verstraete, G. Zerah, J.W. Zwanziger, *Comput. Phys. Comm.* **180**, 2582 (2009).

[19] M. Veithen, X. Gonze, P. Ghosez, *Phys. Rev. B* **71**, 125107 (2005).

[20] J.P. Perdew, K. Burke, M. Ernzerhof, *Phys. Rev. Lett.* **77**, 3865-3868 (1996).

[21] H.J. Monkhorst, J.D. Pack, *Phys. Rev. B* **13**, 5188−5192 (1976).

[22] E. Philippot, P. Armand, P. Yot, O. Cambon, A. Goiffon, G.J. McIntyre, P. Bordet, *Journal of Solid State Chemistry* **146**, 114-123 (1999).

[23] P.D. Battle, A.K. Cheetham, C. Gleitzertt, W.T.A. Harrison, G.J. Long, G. Longworth, *J. Phys. C: Solid State Phys.* **15**, L919-L924 (1982).

[24] J.P. Perdew, Y. Wang, *Phys. Rev. B*. **45**, 13244–13249 (1992).

[25] F. D'Yvoire, M. Ronis, *Comptes rendus de l'Académie des Sciences de Paris* **Série C t.267**, 955-958 (1968).

[26] E.C. Spencer, V.R. Soghomonian, L. Nancy, *Inorg. Chem.* **54**, 7548-7554 (2015).

[27] Y. Xu, G. Zhou, X. Zheng, *Acta Crystallographica E* , *Structure Reports Online* **63**, i67-i69 (2007).

[28] M. Souleiman, O. Cambon, A. Haidoux, J. Haines, C. Levelut, V. Ranieri, J.L. Hazemann, *Inorg. Chem.* **51**, 11811–11819 (2012).

[29] M. O'Keefe, A. Navrotsky, *Academic Press*, New York, (1981).

[30] R.D. Shannon, *Acta Crystallogr. Sect. A Found. Crystallogr.* **32**, 751–767 (1976).

[31] M. Souleiman, P. Hermet, A. Haidoux, C. Levelut, J. Haines, O. Cambon, *RSC Adv*. **3**, 22078–22086 (2013).

[32] J.T. Kloprogge, B.J. Wood, *Spectrochimica Acta Part A* **185**, 163–172 (2017).

[33] M.A. Gomez, J.F. Le Berre, H. Assaaoudi, G.P. Demopoulos, *J. Raman Spectrosc*. **42**, 62–71 (2011).

[34] M.A. Gomez, H. Assaaoudi, L. Becze, J.N. Cutler, G.P. Demopoulos, *J. Raman Spectrosc*. **41**, 212–221 (2010).

[35] K.S. Savage, D.K. Bird, P.A. O'Day, *Chem. Geol*. **215**, 473–498 (2005).

[36] S.C.B. Myneni, S.J. Traina, G.A. Waychunas, T.J. Logan, *Geochim. Cosmochim. Acta.* **62**, 3285– 3300 (1998).

[37] O.A. Aljowder, *Spectrochim. Acta A* **60**, 2837-2841 (2004).

[38] K. Nakamoto, Infrared and Raman spectra of inorganic and coordination compounds. Part A: theory and applications in inorganic chemistry (6th edn). Wiley: New York (2009).

[39] G.M. Bhalerao, P. Hermet, J. Haines, O. Cambon, D.A. Keen, M.G. Tucker, E. Buixaderas, P. Simon, *Phys. Rev. B* **86**, 134104–134112 (2012).

[40] E. Angot, R. Le Parc, C. Levelut, M. Beaurain, P. Armand, O. Cambon, J. Haines, *J. Phys.: Condens. Matter* **18**, 4315-4327 (2006).

[41] O. Cambon, G.M. Bhalerao, D. Bourgogne, J. Haines, P. Hermet, D.A. Keen, M.G. Tucker, *J. Am. Chem. Soc.* **133**, 8048–8056 (2011).

[42] R. Bechmann, *Phys. Rev.* **110**, 1060-1061 (1958).

[43] Bailey, D. S.; Andle, J. C.; Lee, D. L.; Soluch, W.; Vetelino, J. F.; Chai, B. H. T. *in Proceedings of the 1983 IEEE Ultrasonics Symposium* (IEEE, New York, 1983) 335-340.

[44] Philippot, E.; Palmier, D.; Pintard, M.; Goiffon, A. A General Survey of Quartz and Quartz-like Materials: Packing Distortions, Temperature, and Pressure Effects. *J. Solid State Chem.* **123**, 1-13 (1996).

[45] Wallnöfer, W.; Krempl, P. W.; Asenbaum, A. Determination of the Elastic and Photoelastic Constants of Quartz-Type $GaPO_4$ by Brillouin Scattering. *Phys. Rev. B* **49**, 10075-10080 (1994).

[46] Estimation from Fertey, P.; Alle, P.; Wenger, E.; Dinkespiler, B.; Cambon, O; Haines, J.; Hustache, S.; Medjoubi, K.; Picca, F.; Dawiec, A.; Breugnon, P.; Delpierre, P.; Mazzoli, C.; Lecomte, C. Diffraction Studies Under In-Situ Electric Field Using a Large-Area Hybrid Pixel XPAD Detector. *J. Appl. Cryst.* **46**, 1151-1161 (2013).

[47] Unpublished.

[48] Tarumi, R.; Nakamura, K.; Ogi, H.; Hirao, M. Complete Set of Elastic and Piezoelectric Coefficients of α-Quartz at Low Temperatures. J. Appl. Phys. **102**, 113508 (2007).

[49] Bechmann, R. Elastic and Piezoelectric Constants of Alpha-Quartz. Phys. Rev. **110**, 1060-1061 (1958).

[50] Philippot, E.; Ibanez, A.; Goiffon, A.; Cochez, M.; Zarka, A.; Capelle, B.; Schwartzel, J.; Détaint, J. A Quartz-Like Material: Gallium Phosphate ($GaPO_4$); Crystal Growth and Characterization. J. of Crystal Growth **130** 195-208 (1993).